sustainable chemistry

MDPI

Article

Computational Investigation of a NASICON-Type Solid Electrolyte Material $LiGe_2(PO_4)_3$

Navaratnarajah Kuganathan [1,*], Kobiny Antony Rex [2] and Poobalasuntharam Iyngaran [2]

[1] Department of Materials, Faculty of Engineering, Imperial College London, London SW7 2AZ, UK
[2] Department of Chemistry, University of Jaffna, Sir. Pon Ramanathan Road, Thirunelvely, Jaffna 40000, Sri Lanka
* Correspondence: n.kuganathan@imperial.ac.uk

Abstract: Phosphate-based electrolyte materials are of great interest in the field of Li-ion batteries due to their rigid structural integrity. $LiGe_2(PO_4)_3$ is a NASICON-type phosphate material with high thermal and electrochemical stability. Computational simulation techniques were employed to study the defects, diffusion, and dopant properties of $LiGe_2(PO_4)_3$. Furthermore, the reaction energies for the formation of $LiGe_2(PO_4)_3$ and the incorporation energies for the insertion of additional Li into this material were calculated. The calculations revealed that the Li Frenkel is the lowest-energy defect. The second most favorable defect is the Ge-P anti-site defect cluster. A low Li migration energy of 0.44 eV implies high Li ionic conductivity. The most favorable isovalent dopants on the Li and Ge sites are Na and Si, respectively. The formation of Li interstitials and oxygen vacancies can be facilitated through the doping of Ga on the Ge site. The doping of Ga slightly enhances the Li ionic conductivity. Li incorporation (up to four Li) is thermodynamically feasible.

Keywords: $LiGe_2(PO_4)_3$; defects; dopants; DFT simulation; solution energy

Citation: Kuganathan, N.; Rex, K.A.; Iyngaran, P. Computational Investigation of a NASICON-Type Solid Electrolyte Material $LiGe_2(PO_4)_3$. *Sustain. Chem.* **2022**, *3*, 404–414. https://doi.org/10.3390/suschem3030025

Academic Editor: Cristina Pozo-Gonzalo

Received: 11 July 2022
Accepted: 5 September 2022
Published: 7 September 2022

Publisher's Note: MDPI stays neutral with regard to jurisdictional claims in published maps and institutional affiliations.

1. Introduction

There is an ongoing research interest in finding a suitable solid electrolyte material that can be used in lithium ion batteries (LIBs). A variety of solid electrolyte materials, including NASICON-type phosphates [1–3], perovskites [4–6], garnets [7–9], and anti-perovskites [10–12], have been extensively examined.

Lithium germanium phosphate [$LiGe_2(PO_4)_3$] is one of the NASICON-type solid electrolyte materials that has many advantages, such as high electrochemical and thermal stability [13,14]. The high stability is attributed to the stable oxidation state of germanium (IV) in $LiGe_2(PO_4)_3$. Practical application of this material is limited by its low ionic conductivity. Many experimental studies considered single or dual doping of trivalent cations on the Ge site to improve its Li-ion conductivity [15–19]. Such improvement is assisted via the formation of additional Li^+ ions in the lattice. Kotobuki et al. [20] used a co-precipitation method to prepare $Li_{1.5}Al_{0.5}Ge_{1.5}(PO_4)_3$ at high temperatures and observed an enhancement in the Li-ion conductivity. A similar conclusion was reached in other experimental studies, although their methodologies of preparation were different. Nikodimos et al. [15] studied the Li-ion conductivity in Al-Sc dual-doped $LiGe_2(PO_4)_3$ both experimentally and computationally and concluded that a significant enhancement in the ionic conductivity was achieved with the reduction of the activation energy.

Little is known about the defect chemistry of $LiGe_2(PO_4)_3$. Computer modeling techniques are useful for finding the possible intrinsic defects present in this material, Li-ion diffusion pathways and their activation energies, and solutions of a variety of dopants, as discussed in previous simulation studies [21–26]. To this end, we used a classical simulation based on the pair-wise potentials. Furthermore, density functional theory (DFT) simulations were employed to elucidate the electronic structures of $LiGe_2(PO_4)_3$, doped-$LiGe_2(PO_4)_3$, and Li-incorporated $LiGe_2(PO_4)_3$.

2. Computational Methods

The calculations were carried out by using classical pair potentials as implemented in the GULP (General Utility Lattice Program) code [27] and projected augmented wave (PAW) pseudo-potentials [28] as implemented in the VASP (Vienna ab initio Simulation Package) code [29]. The GULP code enabled us to examine the most probable defect energy processes, Li-ion migration pathways, and solutions of dopants. The electronic structures of pristine $LiGe_2(PO_4)_3$ and doped-$LiGe_2(PO_4)_3$ were modeled by using the VASP code.

The GULP code uses ionic interactions, such as long-range attraction (Coulomb) and short-range (Pauli repulsion and van der Waals attraction) forces. The short-range interactions were described using Buckingham potentials (see Table 1) [30,31]. Both lattice constants and ionic positions were relaxed with the aid of the Broyden–Fletcher–Goldfarb–Shanno (BFGS) algorithm [32]. Point defect relaxation was modeled using the Mott–Littleton method [33]. Li-ion diffusion pathways were calculated by considering seven interstitial positions between two local Li vacancy sites. The activation energy was calculated as the energy difference between the local maximum energy along this diffusion pathway and the initial vacancy defect energy.

Table 1. Buckingham potential parameters used in the classical simulations of $LiGe_2(PO_4)_3$ [30,31].

Interaction	*A*/eV	*ρ*/Å	*C*/eV·Å^6	Y/e	K/eV·Å^{-2}
Li^+–O^{2-}	632.1018	0.2906	0.00	1.000	99,999
Ge^{4+}–O^{2-}	1497.3996	0.325646	16.00	4.000	99,999
P^{5+}–O^{2-}	897.2648	0.3577	0.00	5.000	99,999
O^{2-}–O^{2-}	22,764.30	0.1490	44.53	−2.040	65.00

The VASP code uses PAW potentials and plane wave basis sets. The exchange-correlation term was described using the generalized gradient approximation (GGA) as formulated by Perdew, Burke, and Ernzerhof (PBE) [34]. In all cases, a plane wave basis set with a cut-off value of 500 eV was used. A 4 × 4 × 4 Monkhorst–Pack [35] k-point mesh was used to model bulk $LiGe_2(PO_4)_3$. A 2 × 2 × 1 supercell consisting of 432 atoms (Li: 24, Ge: 48, P: 72, and O: 288) was used to model defects. For defect calculations, we used a 2 × 2 × 2 Monkhorst–Pack k-point mesh. The conjugate gradient algorithm [36] was applied to optimize both bulk and defect configurations. The force tolerance was set to be 0.001 eV/Å. The Bader charge analysis [37] was used to estimate the charges on the dopants and incorporated Li atoms.

The two-body expression [$\Phi_{ij}(r_{ij}) = A_{ij} \exp(-r_{ij}/\rho_{ij}) - C_{ij}/r_{ij}^6$] was used, where A, ρ, and C are parameters reproducing the experimental data. The values of Y and K are shell charges and spring constants, respectively.

3. Results

3.1. Crystal Structure of $LiGe_2(PO_4)_3$

$LiGe_2(PO_4)_3$ crystallizes in the rhombohedral space group $R\bar{3}C$ (a = b = 8.275 Å, c = 20.470 Å, α = β = 90° and γ = 180°) [38] and consists of PO_4 tetrahedra and GeO_6 octahedra. These two polyhedrons share their corners, forming a three-dimensional network (see Figure 1a). Both classical and DFT simulations were employed to relax the ionic positions and lattice parameters of $LiGe_2(PO_4)_3$. The calculated lattice parameters were in good agreement with the values reported in the experiment, showing the suitability of the potential parameters, pseudopotentials, and basis sets used in this study (see Table 2).

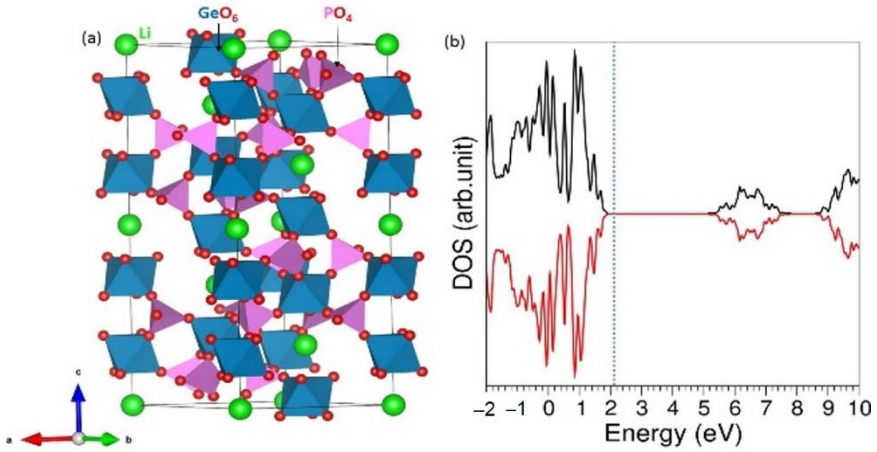

Figure 1. (**a**) Relaxed structure of $LiGe_2(PO_4)_3$ and (**b**) its total DOS plot.

Table 2. Calculated lattice parameters of the $LiGe_2(PO_4)_3$ crystal structure. The corresponding experimental values are also provided for comparison. The vertical blue dotted line shows the Fermi energy level.

Parameter	Experiment [38]	Calculated		|Δ| (%)	
		Classical	DFT	Classical	DFT
a = b (Å)	8.275	8.194	8.386	0.16	1.34
c (Å)	20.470	20.585	20.543	0.56	0.36
α = β (°)	90.0	90.0	90.0	0.00	0.00
γ (°)	120.0	0.00	120.0	0.00	0.00

The electronic structure calculation performed by using DFT showed that $LiGe_2(PO_4)_3$ is an insulator with a band gap of 3.50 eV (see Figure 1b). The value calculated in this study is in a good agreement with a value (3.38 eV) reported in a previous DFT simulation study [39].

3.2. Defect Properties

In this section, the formation of intrinsic defect processes such as Frenkel, Schottky, and anti-site defects, is discussed. Initially, the point defect energies were calculated, and then they were combined to calculate the intrinsic defect processes with the appropriate energies of the lattices. The following equations were written using Kröger–Vink notation [40] to explain the defect reactions. Anti-site defects were considered to be in an isolated or clustered form. Isolated anti-site defects were modeled by considering defects separately. In the clustered form, defects were considered in the same supercell.

$$\text{Li Frenkel} : \mathrm{Li}_{\mathrm{Li}}^{\mathrm{X}} \rightarrow \mathrm{V}_{\mathrm{Li}}^{\prime} + \mathrm{Li}_{\mathrm{i}}^{\bullet} \quad (1)$$

$$\text{Ge Frenkel} : \mathrm{Ge}_{\mathrm{Ge}}^{\mathrm{X}} \rightarrow \mathrm{V}_{\mathrm{Ge}}^{\prime\prime\prime\prime} + \mathrm{Ge}_{\mathrm{i}}^{\bullet\bullet\bullet\bullet} \quad (2)$$

$$\text{O Frenkel} : \mathrm{O}_{\mathrm{O}}^{\mathrm{X}} \rightarrow \mathrm{V}_{\mathrm{O}}^{\bullet\bullet} + \mathrm{O}_{\mathrm{i}}^{\prime\prime} \quad (3)$$

$$\text{P Frenkel} : \mathrm{P}_{\mathrm{P}}^{\mathrm{X}} \rightarrow \mathrm{V}_{\mathrm{P}}^{\prime\prime\prime\prime\prime} + \mathrm{P}_{\mathrm{i}}^{\bullet\bullet\bullet\bullet\bullet} \quad (4)$$

$$\text{Schottky} : \mathrm{Li}_{\mathrm{Li}}^{\mathrm{X}} + 2\mathrm{Ge}_{\mathrm{Ge}}^{\mathrm{X}} + 3\mathrm{P}_{\mathrm{P}}^{\mathrm{X}} + 12\mathrm{O}_{\mathrm{O}}^{\mathrm{X}} \rightarrow \mathrm{V}_{\mathrm{Li}}^{\prime} + 2\mathrm{V}_{\mathrm{Ge}}^{\prime\prime\prime\prime} + 3\mathrm{V}_{\mathrm{P}}^{\prime\prime\prime\prime\prime} + 12\mathrm{V}_{\mathrm{O}}^{\bullet\bullet} + \mathrm{LiGe}_2(\mathrm{PO}_4)_3 \quad (5)$$

$$\mathrm{Li_2O\ Schottky} : 2\mathrm{Li}_{\mathrm{Li}}^{\mathrm{X}} + \mathrm{O}_{\mathrm{O}}^{\mathrm{X}} \rightarrow 2\mathrm{V}_{\mathrm{Li}}^{\prime} + \mathrm{V}_{\mathrm{O}}^{\bullet\bullet} + \mathrm{Li_2O} \quad (6)$$

$$\mathrm{GeO_2\ Schottky} : \mathrm{Ge}_{\mathrm{Ge}}^{\mathrm{X}} + 2\mathrm{O}_{\mathrm{O}}^{\mathrm{X}} \rightarrow \mathrm{V}_{\mathrm{Ge}}^{\prime\prime\prime\prime} + 2\,\mathrm{V}_{\mathrm{O}}^{\bullet\bullet} + \mathrm{GeO_2} \quad (7)$$

$$\text{Li/Ge antisite (isolated)} : \mathrm{Li}_{\mathrm{Li}}^{\mathrm{X}} + \mathrm{Ge}_{\mathrm{Ge}}^{\mathrm{X}} \rightarrow \mathrm{Li}_{\mathrm{Ge}}^{\prime\prime\prime} + \mathrm{Ge}_{\mathrm{Li}}^{\bullet\bullet\bullet} \quad (8)$$

$$\text{Li/Ge antisite (cluster)} : \mathrm{Li}_{\mathrm{Li}}^{\mathrm{X}} + \mathrm{Ge}_{\mathrm{Ge}}^{\mathrm{X}} \rightarrow \left\{\mathrm{Li}_{\mathrm{Ge}}^{\prime\prime\prime} : \mathrm{Ge}_{\mathrm{Li}}^{\bullet\bullet\bullet}\right\}^{\mathrm{X}} \quad (9)$$

$$\text{Ge/P antisite (isolated)} \ : \ Ge_{Ge}^{X} + P_{P}^{X} \rightarrow Ge_{P}^{\prime} + P_{Ge}^{\bullet} \quad (10)$$

$$\text{Ge/P antisite (cluster)} \ : \ Ge_{Ge}^{X} + P_{P}^{X} \rightarrow \left\{Ge_{P}^{\prime} : P_{Ge}^{\bullet}\right\}^{X} \quad (11)$$

Table 3 reports the calculated defect energies. The calculations show that the most prominent defect in this material was the Li Frenkel defect (0.75 eV/defect). The concentration of this defect was higher than those of the other defect processes. In particular, Li vacancies in the material facilitate vacancy-assisted Li-ion migration. The second most favorable defect was the Ge-P anti-site defect cluster (1.26 eV/defect). This defect cluster was formed by the aggregation of isolated defects with a binding energy of −0.75 eV. Anti-site defects have been observed in many as-prepared oxide materials [41–43]. Both experimental and theoretical studies have shown that this defect would change the properties of materials [44–46]. The Li-Ge anti-site defect energy was high due to the charge difference between Li^{+} and Ge^{4+}. The Li_2O partial Schottky energy was relatively low (3.10 eV/defect). Other Frenkel and Schottky defect energies were high (>4 eV), meaning that the defects were not significant in this material at room temperature.

Table 3. Calculated defect energies of intrinsic defects.

Reaction Equation	Reaction Energy (eV)	Reaction Energy (eV)/Defect
1	1.50	0.75
2	22.36	11.18
3	8.12	4.06
4	32.26	16.13
5	124.56	6.92
6	9.30	3.10
7	22.29	7.43
8	17.86	8.93
9	6.56	3.28
10	4.02	2.01
11	2.52	1.26

3.3. Diffusion of Li Ions

Materials that exhibit a high Li-ionic conductivity are important in the construction of promising Li-ion batteries. The experimental determination of long-range Li-ion diffusion pathways is generally challenging. Computational simulation studies have been useful in predicting the diffusion pathways or validating the pathways determined in experimental studies. For example, the Li-ion diffusion pathway and its migration barrier in $Li_{1+x}Al_xTi_{2-x}(PO_4)_3$ as calculated by Case et al. [47] were in excellent agreement with the corresponding experimental observations [19,48].

Here, a classical simulation was employed to examine the diffusion of Li ions. We identified a local Li hop with a jump distance of 5.89 Å and calculated its vacancy-assisted migration pathway and activation energy. The activation energy for this hop was 0.44 eV. This Li hop was extended through the lattice to construct a long-range Li-ion diffusion pathway. This resulted in a three-dimensional pathway, as shown in Figure 2a. The energy profile diagram (see Figure 2b) shows the activation energy calculated for this local Li hop. As this long-range diffusion pathway consisted of only one Li hop, the overall migration barrier was also 0.44 eV. The experimental activation energy of the Li ions in $LiGe_2(PO_4)_3$ reported by Martínez-Juárez et al. [49] was 0.60 eV. In another experimental study by Nikodimos et al. [15], it was reported that the activation energy was 0.286 eV, and the DFT-based calculation by the same authors revealed an activation energy of 0.329 eV. The activation energy calculated in this study was between two experimental values and was closer to the value calculated in the DFT simulation. Nevertheless, this material exhibited high Li-ion conductivity.

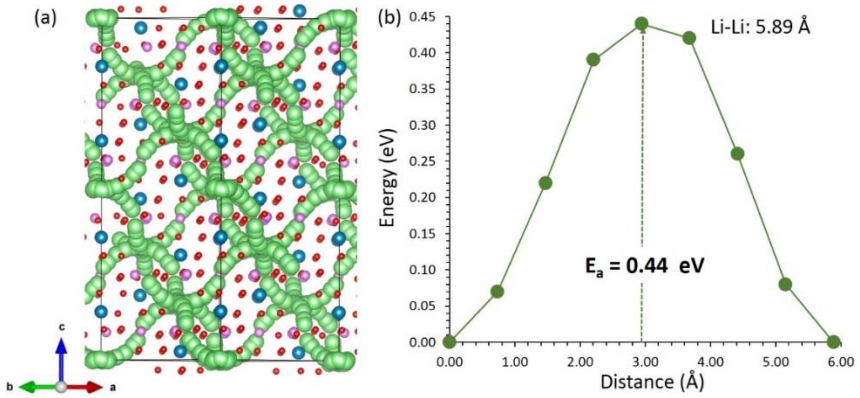

Figure 2. (**a**) Long-range Li-ion diffusion pathway and (**b**) an energy profile diagram showing the activation energy.

3.4. Solutions of Dopants

Ionic dopants are generally used to increase the ionic conductivity and chemical and mechanical stability of materials. Here, we considered a range of dopants to screen and predicted promising dopants that can be of interest for future experiments. For the dopant calculations, a classical simulation was employed. Charge-compensating defects, such as interstitials, vacancies, and lattice energies, were used to calculate solution energies. In the electronic supplementary information (ESI), the Buckingham potentials used for the oxides of dopants are listed (see Table S1).

First, alkali dopants (M = Na, K and Rb) on the Li site were considered. The following reaction equation explains the doping process.

$$\frac{1}{2}M_2O + Li_{Li}^{X} \rightarrow M_{Li}^{X} + \frac{1}{2}Li_2 \quad (12)$$

The most favorable dopant was Na^+, with an exothermic solution energy of −0.90 eV (Table 4). This was due to the ionic radius of Na^+, which is close to that of Li^+ (0.76 Å). There was a gradual increase in the solution energy with the increase in the ionic radii of the dopants. Both K^+ and Rb^+ ions exhibited endoergic solution energies. A possible doped configuration that can be synthesized is $Li_{1-x}Na_xGe_2(PO_4)_3$ (x = 0.0–1.0).

Table 4. Solution energies calculated for alkali dopants on the Li site.

Dopant Ions	Ionic Radius of Dopant Ion (Å)	Solution Energy (eV)/Dopant
Na^+	1.02	−0.90
K^+	1.38	0.42
Rb^+	1.52	1.77

The relaxed structure of Na-doped $LiGe_2(PO_4)_3$ is shown Figure 3a. The doped Na atom forms a distorted octahedral structure (NaO_6) with longer Na-O bond distances than Li-O bond distances in the LiO_6 octahedral structure. As mentioned earlier, this is due to the fact that the ionic radius of Na^+ is larger than that of Li^+. The DOS plots show that the doping had a negligible impact on the electronic structure and that there were no additional states present in the gap.

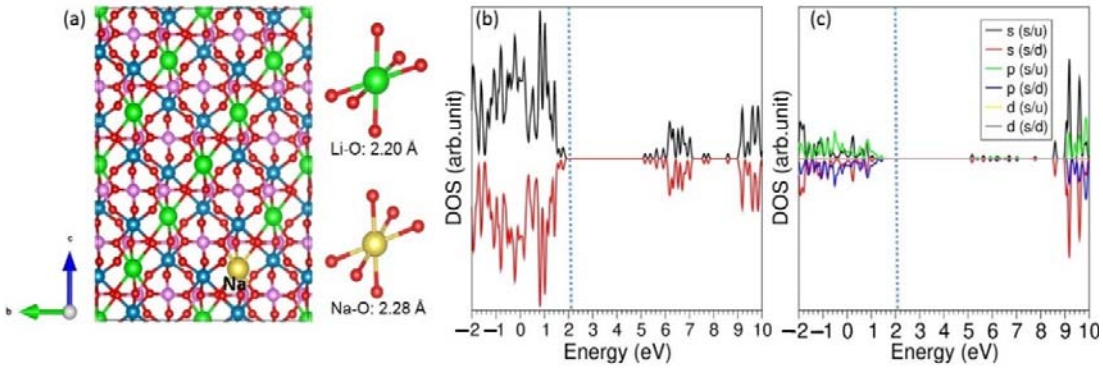

Figure 3. (**a**) Relaxed structure of Na-doped $LiGe_2(PO_4)_3$, (**b**) total DOS plot of the doped structure, and (**c**) atomic DOS plot of Na.

Next, we considered the doping of trivalent dopants (M = Al, Ga, Sc, In, Y, Gd, and La) on the Ge site. This doping process can create additional Li in the form of interstitials in the lattice according to the following equation. The presence of additional Li can increase the capacity of batteries.

$$M_2O_3 + 2\,Ge_{Ge}^{X} + \ Li_2O \rightarrow \ 2\,M'_{Ge} + 2\,Li_i^{\bullet} + 2\,GeO_2 \tag{13}$$

The most promising dopant was Ga^{3+}, and the solution energy for this dopant was 2.20 eV (see Table 5). The solution energy calculated for Al^{3+} was higher than that calculated for Ga^{3+} by only 0.14 eV. The favorability of both dopants (Ga^{3+} and Al^{3+}) was due to the fact that their ionic radii matched closely with the ionic radius of Ge^{4+} (0.53 Å). The solution energy gradually increased with the increase in the ionic radius. The most unfavorable dopant was La^{3+}, and its solution energy was 4.28 eV.

Table 5. Solution energies calculated for trivalent dopants on the Ge site producing Li interstitials and oxygen vacancies.

Dopant Ions	Ionic Radius of Dopant Ion (Å)	Solution Energy (eV)/Dopant	
		$Li_i^{\bullet}$	$V_O^{\bullet\bullet}$
Al^{3+}	0.54	2.34	5.49
Ga^{3+}	0.62	2.20	5.34
Sc^{3+}	0.75	2.58	5.72
In^{3+}	0.80	2.82	5.97
Y^{3+}	0.90	3.36	6.50
Gd^{3+}	0.94	3.75	6.89
La^{3+}	1.03	4.28	7.42

The same doping process can introduce oxygen vacancies, as explained in the following reaction equation.

$$M_2O_3 + 2\,Ge_{Ge}^{X} + \ O_O^{X} \rightarrow \ 2\,M'_{Ge} + \ V_O^{\bullet\bullet} + 2\,GeO_2 \tag{14}$$

The solution energies were higher for this process than those calculated for the process in which Li interstitials acted as charge-compensating defects (see Equation (13)). This indicates that the concentration of oxygen vacancies will not be high at room temperature. Although the solution energies were larger than 5 eV for all dopants, the candidate dopant was Ga^{3+}. The trend in the solution energy was the same as that calculated for the previous process.

The relaxed structures of Ga-doped $LiGe_2(PO_4)_3$ and electronic structures are shown in Figure 4. The Ga-O bond distances in the GaO_6 octahedral unit were larger than the Ge-O bond distances. The band-gap value was not altered much upon doping. The atomic

DOS plots show that states arising from Ga were mainly localized in the valence band (see Figure 4c,f).

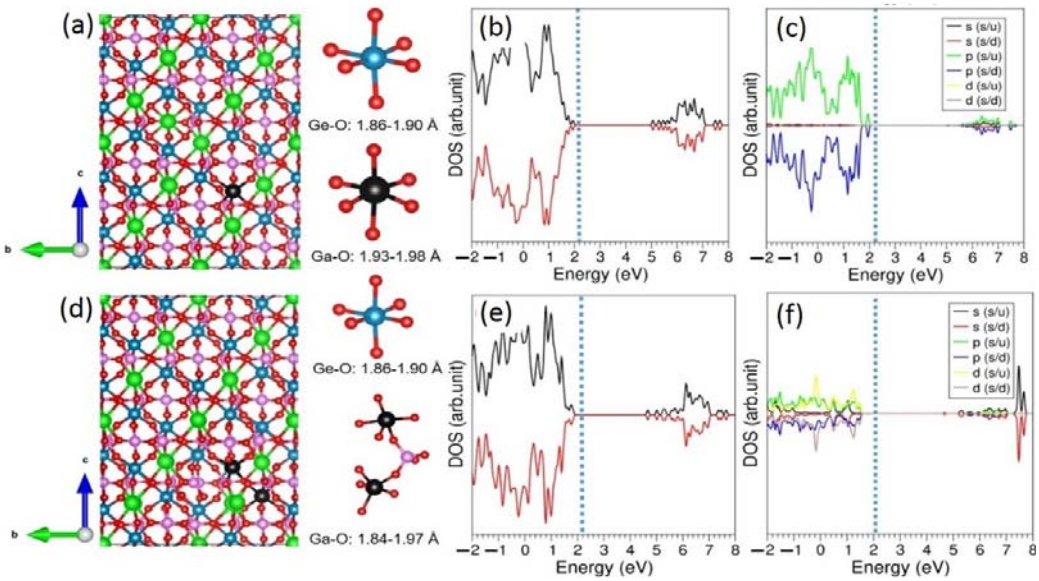

Figure 4. (**a**) Relaxed structure of Ga-doped $LiGe_2(PO_4)_3$ forming Li interstitials, (**b**) total DOS plot of the doped structure, and (**c**) atomic DOS plot of Ga. The corresponding figures (**d**–**f**) plotted for Ga-doped $LiGe_2(PO_4)_3$ forming oxygen vacancies are also shown.

Finally, tetravalent dopants (Si, Ti, Sn, Zr, and Ce) were substitutionally doped on the Ge site. The solution energies were calculated using the following equation.

$$MO_2 + Ge_{Ge}^{X} \rightarrow M_{Ge}^{X} + GeO_2 \quad (15)$$

The solution energy calculated for Si^{4+} was 0.67 eV (see Table 6). The other dopants exhibited higher solution energies. Thus, Si^{4+} was the most promising. This was partly due to the fact that the ionic radius of Si^{4+} closely matched with that calculated for Ge^{4+}. The next most favorable dopant was Ti^{4+}. Its solution energy was almost double the solution energy calculated for Si^{4+}. Both Sn^{4+} and Zr^{4+} had solution energies that were closer to each other. The solution energy calculated for Ce^{4+} was highly endoergic, and the doping of this cation required a high temperature.

Table 6. Solution energies calculated for tetravalent dopants on the Ge site.

Dopant Ions	Ionic Radius of Dopant Ion (Å)	Solution Energy (eV)/Dopant
Si^{4+}	0.40	0.67
Ti^{4+}	0.61	1.26
Sn^{4+}	0.69	1.64
Zr^{4+}	0.72	1.67
Ce^{4+}	0.87	3.42

The relaxed structure of Si-doped $LiGe_2(PO_4)_3$ and its electronic structure are shown in Figure 5. The Si-O bond distances in SiO_6 unit are shorter than Ge-O bond distances in GeO_6 unit. This is partly owing to the fact that the ionic radius of Si^{4+} (0.40 Å) is smaller than that of Ge^{4+} (0.53 Å). The total and atomic DOS plots show that the insulating nature of this material is unchanged.

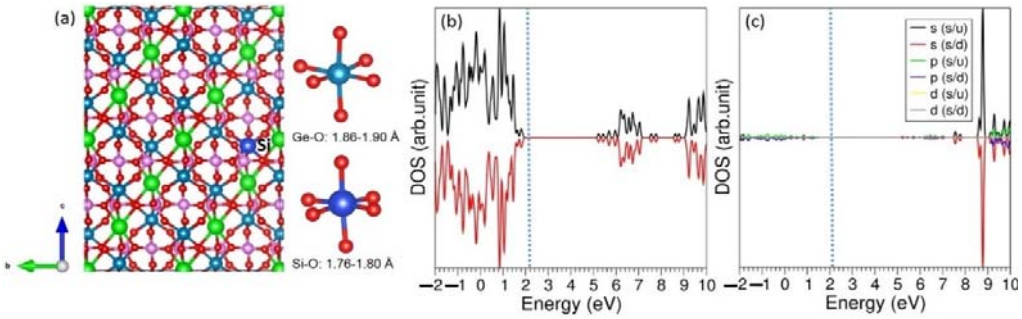

Figure 5. (**a**) Relaxed structure of Si-doped $LiGe_2(PO_4)_3$, (**b**) total DOS plot of the doped structure, and (**c**) atomic DOS plot of Si.

3.5. Diffusion of Li Ions in Ga-Doped $LiGe_2(PO_4)_3$

The migration energy was calculated for a local Li hop in the presence of Ga on the Ge site. The migration energy was calculated to be 0.39 eV. The dopant concentration was 2.08%. It is expected that the migration energy can be decreased with further substitution.

3.6. Li Incorporation

The incorporation of extra lithium was considered by calculating the incorporation energies with respect to a Li atom and bulk Li. Table 7 reports the incorporation energies, Bader charges on the incorporated Li atoms, and volume changes upon Li incorporation. The incorporation energies were negative in all cases with respect to both a Li atom and bulk Li as reference states. The incorporation energies calculated with respect to the bulk Li were less exothermic. This was partly due to the additional energy needed to dissociate bulk Li to form Li atoms. The Bader charge analysis showed that all incorporated Li atoms became single positively charged ions (Li^+). The formation of positively charged ions was due to the strong Li-O bond formation with the nearest neighboring oxygen ions in the lattice (see Figure 6a–d). The incorporation became stronger with increase in the concentration of Li atoms. This enhancement in the incorporation was facilitated by the expansion of the volume.

Table 7. Incorporation energies, Bader charges on the incorporated Li atoms, and volume changes upon subsequent incorporation of Li atoms into $LiGe_2(PO_4)_3$.

Reaction	Incorporation Energy (eV)/Li		Bader Charge (|e|)	$\frac{\Delta V}{V}$ (%)
	Ref: Li Atom	Ref: Li Bulk		
$Li + LiGe_2(PO_4)_3 \rightarrow Li\bullet\ LiGe_2(PO_4)_3$	–2.08	–0.47	+1.00	0.30
$2\ Li + LiGe_2(PO_4)_3 \rightarrow 2\ Li\bullet\ LiGe_2(PO_4)_3$	–2.53	–0.92	+1.00 (2)	0.56
$3\ Li + LiGe_2(PO_4)_3 \rightarrow 3\ Li\bullet\ LiGe_2(PO_4)_3$	–2.98	–1.38	+1.00 (3)	0.58
$4\ Li + LiGe_2(PO_4)_3 \rightarrow 4–\ Li\bullet\ LiGe_2(PO_4)_3$	–3.23	–1.62	+1.00 (4)	0.46

DOS plots were constructed for the Li-incorporated structures. The gap region consisted of states associated with the incorporated Li, as evidenced by the atomic DOS plots (see Figure 6i–l). Incorporation slightly reduced the band gap without changing the insulating character of this material.

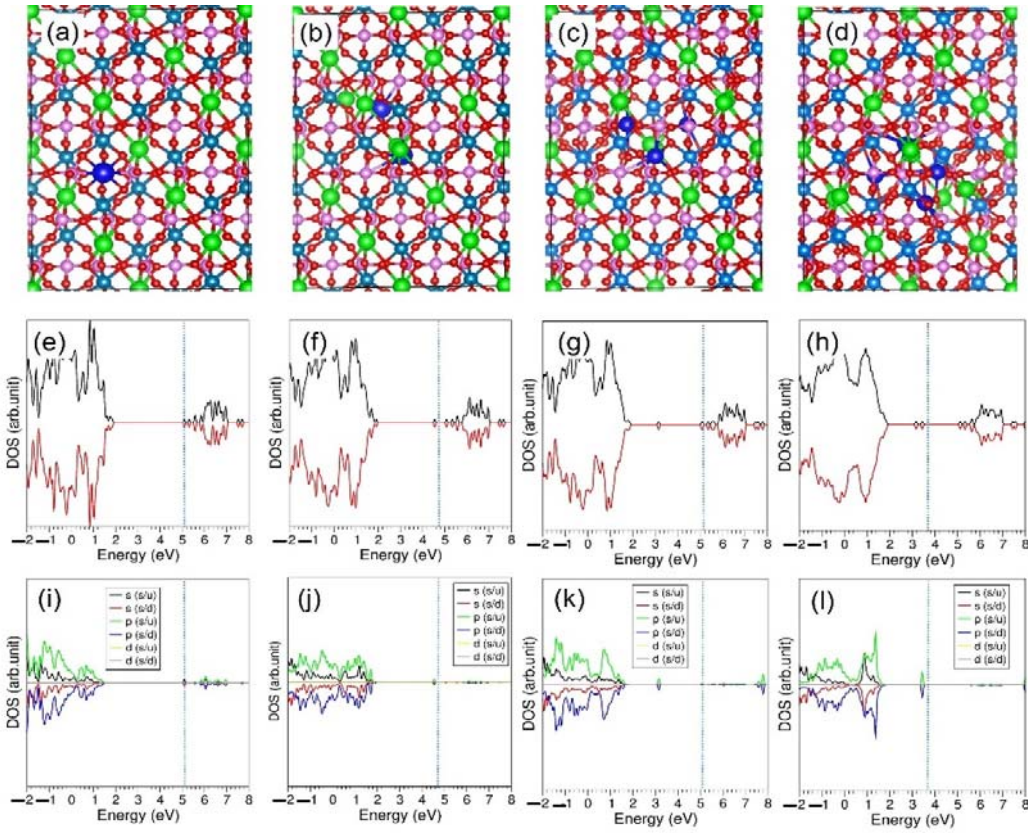

Figure 6. Relaxed structures and $LiGe_2(PO_4)_3$ incorporated with (**a**) a single Li atom, (**b**) two Li atoms, (**c**) three Li atoms, and (**d**) four Li atoms. The corresponding total DOS plots (**e**–**h**) and atomic DOS plots (**i**–**l**) of Li are also shown.

4. Conclusions

This work focused on the computational characterization of defects, diffusion, solutions of dopants, reaction energies for the formation of $LiGe_2(PO_4)_3$, and the energetics of the incorporation of Li into $LiGe_2(PO_4)_3$. The Li Frenkel defect was found to be the most favorable defect in this material, indicating that the concentration of Li vacancies would be higher than those of the other vacancies. The diffusion of Li-ions is three dimensional and fast, with an activation energy of 0.44 eV. The Li and Ge sites were favorably doped by Na and Si, respectively. Doping of Ga on the Ge site can produce Li interstitials or oxygen vacancies as charge-compensating defects. There is a slight improvement in the diffusion of Li^+ ions upon Ga doping on the Ge site. Incorporation of Li is exoergic and becomes more exothermic with the concentration of Li.

Supplementary Materials: The following supporting information can be downloaded at: https://www.mdpi.com/article/10.3390/suschem3030025/s1, Table S1: Two-body Buckingham potentials used for dopant oxides in $LiGe_2(PO_4)_3$.

Author Contributions: Conceptualization, N.K. and K.A.R.; methodology, N.K. and K.A.R.; formal analysis, N.K. and K.A.R.; investigation, N.K.; writing—original draft preparation, N.K.; writing—review and editing, N.K. and P.I.; supervision, N.K.; project administration, N.K. All authors have read and agreed to the published version of the manuscript.

Funding: This research received no external funding.

Institutional Review Board Statement: Not applicable.

Informed Consent Statement: Not applicable.

Data Availability Statement: Not applicable.

Acknowledgments: We acknowledge the high-performance computing center at Imperial College London for their support throughout this project.

Conflicts of Interest: The author declares no conflict of interest.

References

1. Hou, M.J.; Liang, F.; Chen, K.; Dai, Y.N.; Xue, D. Challenges and perspectives of NASICON-type solid electrolytes for all-solid-state lithium batteries. *Nanotechnology* **2020**, *31*, 132003. [CrossRef] [PubMed]
2. El-Shinawi, H.; Regoutz, A.; Payne, D.J.; Cussen, E.J.; Corr, S.A. NASICON $LiM_2(PO_4)_3$ electrolyte (M = Zr) and electrode (M = Ti) materials for all solid-state Li-ion batteries with high total conductivity and low interfacial resistance. *J. Mater. Chem. A* **2018**, *6*, 5296–5303. [CrossRef]
3. He, L.; Oh, J.A.S.; Watarai, K.; Morita, M.; Zhao, Y.; Sun, Q.; Sakamoto, T.; Lu, L.; Adams, S. Electromechanical Failure of NASICON-Type Solid-State Electrolyte-Based All-Solid-State Li-Ion Batteries. *Chem. Mater.* **2021**, *33*, 6841–6852. [CrossRef]
4. Lu, J.; Li, Y. Perovskite-type Li-ion solid electrolytes: A review. *J. Mater. Sci. Mater. Electron.* **2021**, *32*, 9736–9754. [CrossRef]
5. Yan, S.; Yim, C.-H.; Pankov, V.; Bauer, M.; Baranova, E.; Weck, A.; Merati, A.; Abu-Lebdeh, Y. Perovskite Solid-State Electrolytes for Lithium Metal Batteries. *Batteries* **2021**, *7*, 75. [CrossRef]
6. Tewari, N.; Lam, D.; Li, C.H.A.; Halpert, J.E. Recent advancements in batteries and photo-batteries using metal halide per-ovskites. *APL Mater.* **2022**, *10*, 040905. [CrossRef]
7. Kim, A.; Woo, S.; Kang, M.; Park, H.; Kang, B. Research Progresses of Garnet-Type Solid Electrolytes for Developing All-Solid-State Li Batteries. *Front. Chem.* **2020**, *8*, 468. [CrossRef] [PubMed]
8. Kravchyk, K.V.; Zhang, H.; Okur, F.; Kovalenko, M.V. Li–Garnet Solid-State Batteries with LLZO Scaffolds. *Acc. Mater. Res.* **2022**, *3*, 411–415. [CrossRef]
9. Kuganathan, N.; Rushton, M.J.D.; Grimes, R.W.; Kilner, J.A.; Gkanas, E.I.; Chroneos, A. Self-diffusion in garnet-type $Li_7La_3Zr_2O_{12}$ solid electrolytes. *Sci. Rep.* **2021**, *11*, 451. [CrossRef] [PubMed]
10. Dawson, J.A.; Famprikis, T.; Johnston, K.E. Anti-perovskites for solid-state batteries: Recent developments, current challenges and future prospects. *J. Mater. Chem. A* **2021**, *9*, 18746–18772. [CrossRef]
11. Deng, Z.; Ni, D.; Chen, D.; Bian, Y.; Li, S.; Wang, Z.; Zhao, Y. Anti-perovskite materials for energy storage batteries. *InfoMat* **2021**, *4*, e12252. [CrossRef]
12. Yu, P.; Ye, Y.; Zhu, J.; Xia, W.; Zhao, Y. Optimized Interfaces in Anti-Perovskite Electrolyte-Based Solid-State Lithium Metal Batteries for Enhanced Performance. *Front. Chem.* **2021**, *9*, 786956. [CrossRef]
13. Ling, J.; Karuppiah, C.; Krishnan, S.G.; Reddy, M.V.; Misnon, I.I.; Ab Rahim, M.H.; Yang, C.-C.; Jose, R. Phosphate Polyanion Materials as High-Voltage Lithium-Ion Battery Cathode: A Review. *Energy Fuels* **2021**, *35*, 10428–10450. [CrossRef]
14. Chen, A.; Qu, C.; Shi, Y.; Shi, F. Manufacturing Strategies for Solid Electrolyte in Batteries. *Front. Energy Res.* **2020**, *8*, 571440. [CrossRef]
15. Nikodimos, Y.; Tsai, M.-C.; Abrha, L.H.; Weldeyohannis, H.H.; Chiu, S.-F.; Bezabh, H.K.; Shitaw, K.N.; Fenta, F.W.; Wu, S.-H.; Su, W.N.; et al. Al–Sc dual-doped $LiGe_2(PO_4)_3$–A NASICON-type solid electrolyte with improved ionic conductivity. *J. Mater. Chem. A* **2020**, *8*, 11302–11313. [CrossRef]
16. Yamamoto, H.; Tabuchi, M.; Takeuchi, T.; Kageyama, H.; Nakamura, O. Ionic conductivity enhancement in $LiGe_2(PO_4)_3$ solid electrolyte. *J. Power Sources* **1997**, *68*, 397–401. [CrossRef]
17. Xu, H.; Wang, S.; Wilson, H.; Zhao, F.; Manthiram, A. Y-Doped NASICON-type $LiZr_2(PO_4)_3$ Solid Electrolytes for Lithi-um-Metal Batteries. *Chem. Mater.* **2017**, *29*, 7206–7212. [CrossRef]
18. Kang, J.; Chung, H.; Doh, C.; Kang, B.; Han, B. Integrated study of first principles calculations and experimental measurements for Li-ionic conductivity in Al-doped solid-state $LiGe_2(PO_4)_3$ electrolyte. *J. Power Sources* **2015**, *293*, 11–16. [CrossRef]
19. Xu, X.; Wen, Z.; Wu, J.; Yang, X. Preparation and electrical properties of NASICON-type structured $Li_{1.4}Al_{0.4}Ti_{1.6}(PO_4)_3$ glass-ceramics by the citric acid-assisted sol–gel method. *Solid State Ion.* **2007**, *178*, 29–34. [CrossRef]
20. Kotobuki, M.; Koishi, M. Preparation of $Li_{1.5}Al_{0.5}Ge_{1.5}(PO_4)_3$ solid electrolytes via the co-precipitation method. *J. Asian Ceram. Soc.* **2019**, *7*, 551–557. [CrossRef]
21. Kuganathan, N.; Ganeshalingam, S.; Chroneos, A. Defects, Dopants and Lithium Mobility in $Li_9V_3(P_2O_7)_3(PO_4)_2$. *Sci. Rep.* **2018**, *8*, 8140. [CrossRef] [PubMed]
22. Kuganathan, N.; Kordatos, A.; Anurakavan, S.; Iyngaran, P.; Chroneos, A. Li_3SbO_4 lithium-ion battery material: Defects, lithium ion diffusion and tetravalent dopants. *Mater. Chem. Phys.* **2018**, *225*, 34–41. [CrossRef]
23. Kuganathan, N.; Chroneos, A. $Na_3V(PO_4)_2$ cathode material for Na ion batteries: Defects, dopants and Na diffusion. *Solid State Ion.* **2019**, *336*, 75–79. [CrossRef]
24. Pandey, R.; Gale, J.D.; Sampath, S.K.; Recio, J.M. Atomistic Simulation Study of Spinel Oxides: Zinc Aluminate and Zinc Gallate. *J. Am. Ceram. Soc.* **2004**, *82*, 3337–3341. [CrossRef]
25. Zapol, P.; Pandey, R.; Ohmer, M.; Gale, J. Atomistic calculations of defects in $ZnGeP_2$. *J. Appl. Phys.* **1996**, *79*, 671. [CrossRef]
26. Cygan, R.T.; Wright, K.; Fisler, D.K.; Gale, J.D.; Slater, B. Atomistic models of carbonate minerals: Bulk and surface structures, defects, and diffusion. *Mol. Simul.* **2002**, *28*, 475–495. [CrossRef]

27. Gale, J.D. GULP: A computer program for the symmetry-adapted simulation of solids. *J. Chem. Soc. Faraday Trans.* **1997**, *93*, 629–637. [CrossRef]
28. Blöchl, P.E. Projector augmented-wave method. *Phys. Rev. B Condens. Matter Mater. Phys.* **1994**, *50*, 17953–17979. [CrossRef] [PubMed]
29. Kresse, G.; Furthmüller, J. Efficient iterative schemes for ab initio total-energy calculations using a plane-wave basis set. *Phys. Rev. B* **1996**, *54*, 11169–11186. [CrossRef] [PubMed]
30. Islam, M.S.; Driscoll, D.J.; Fisher, C.A.J.; Slater, P.R. Atomic-Scale Investigation of Defects, Dopants, and Lithium Transport in the LiFePO4 Olivine-Type Battery Material. *Chem. Mater.* **2005**, *17*, 5085–5092.
31. Sastre, G.; Gale, J.D. Derivation of an Interatomic Potential for Germanium- and Silicon-Containing Zeolites and Its Application to the Study of the Structures of Octadecasil, ASU-7, and ASU-9 Materials. *Chem. Mater.* **2003**, *15*, 1788–1796. [CrossRef]
32. Gale, J.D.; Rohl, A.L. The General Utility Lattice Program (GULP). *Mol. Simul.* **2003**, *29*, 291–341. [CrossRef]
33. Mott, N.F.; Littleton, M.J. Conduction in polar crystals. I. Electrolytic conduction in solid salts. *Trans. Faraday Soc.* **1938**, *34*, 485–499. [CrossRef]
34. Perdew, J.P.; Burke, K.; Ernzerhof, M. Generalized gradient approximation made simple. *Phys. Rev. Lett.* **1996**, *77*, 3865. [CrossRef] [PubMed]
35. Monkhorst, H.J.; Pack, J.D. Special points for Brillouin-zone integrations. *Phys. Rev. B* **1976**, *13*, 5188. [CrossRef]
36. Press, W.H.; Teukolsky, S.A.; Vetterling, W.T.; Flannery, B.P. Numerical recipes in C. In *The Art of Scientific Computing*, 2nd ed.; Cambridge University Press: Cambridge, UK, 1992.
37. Bader, R.F.W. The zero-flux surface and the topological and quantum definitions of an atom in a molecule. *Theor. Chim. Acta* **2001**, *105*, 276–283. [CrossRef]
38. Alami, M.; Brochu, R.; Soubeyroux, J.; Gravereau, P.; Le Flem, G.; Hagenmuller, P. Structure and thermal expansion of $LiGe_2(PO_4)_3$. *J. Solid State Chem.* **1991**, *90*, 185–193. [CrossRef]
39. The Materials Project. *Materials Data on LiZr2(PO4)3 by Materials Project*; Lawrence Berkeley National Lab. (LBNL): Berkeley, CA, USA, 2020.
40. Kröger, F.A.; Vink, H.J. Relations between the Concentrations of Imperfections in Crystalline Solids. In *Solid State Physics*; Seitz, F., Turnbull, D., Eds.; Academic Press: Cambridge, MA, USA, 1956; Volume 3, pp. 307–435.
41. Lin, Q.; Guan, W.; Zhou, J.; Meng, J.; Huang, W.; Chen, T.; Gao, Q.; Wei, X.; Zeng, Y.; Li, J.; et al. Ni–Li anti-site defect induced intragranular cracking in Ni-rich layer-structured cathode. *Nano Energy* **2020**, *76*, 105021. [CrossRef]
42. Yin, L.; Li, Z.; Mattei, G.S.; Zheng, J.; Zhao, W.; Omenya, F.; Fang, C.; Li, W.; Li, J.; Xie, Q.; et al. Thermodynamics of Antisite Defects in Layered NMC Cathodes: Systematic Insights from High-Precision Powder Diffraction Analyses. *Chem. Mater.* **2019**, *32*, 1002–1010. [CrossRef]
43. Devaraju, M.K.; Truong, Q.D.; Hyodo, H.; Sasaki, Y.; Honma, I. Synthesis, characterization and observation of antisite defects in $LiNiPO_4$ nanomaterials. *Sci. Rep.* **2015**, *5*, 11041. [CrossRef] [PubMed]
44. Düvel, A.; Morgan, L.M.; Chandran, C.V.; Heitjans, P.; Sayle, D.C. Formation and Elimination of Anti-site Defects during Crystallization in Perovskite $Ba_{1-x}Sr_xLiF_3$. *Cryst. Growth Des.* **2018**, *18*, 2093–2099. [CrossRef]
45. Bandaru, S.; Katre, A.; Carrete, J.; Mingo, N.; Jund, P.; Montaña, J.C. Influence of Antisite Defects on the Thermoelectric Properties of Fe_2VAl. *Nanoscale Microscale Thermophys. Eng.* **2017**, *21*, 237–246. [CrossRef]
46. Feng, Z.; Zhang, J.; Yan, Y.; Zhang, G.; Wang, C.; Peng, C.; Ren, F.; Wang, Y.; Chen, Z. Ag-Mg antisite defect induced high thermoelectric performance of α-MgAgSb. *Sci. Rep.* **2017**, *7*, 2572. [PubMed]
47. Case, D.; McSloy, A.J.; Sharpe, R.; Yeandel, S.R.; Bartlett, T.; Cookson, J.; Dashjav, E.; Tietz, F.; Kumar, C.M.N.; Goddard, P. Structure and ion transport of lithium-rich $Li_{1+x}Al_xTi_{2-x}(PO_4)_3$ with 0.3<x<0.5: A combined computational and experimental study. *Solid State Ion.* **2020**, *346*, 115192.
48. Wang, C.; Sun, Q.; Liu, Y.; Zhao, Y.; Li, X.; Lin, X.; Banis, M.N.; Li, M.; Li, W.; Adair, K.R.; et al. Boosting the performance of lithium batteries with solid-liquid hybrid electrolytes: Interfacial properties and effects of liquid electrolytes. *Nano Energy* **2018**, *48*, 35–43. [CrossRef]
49. Martínez-Juárez, A.; Pecharromán, C.; Iglesias, J.E.; Rojo, J.M. Relationship between Activation Energy and Bottleneck Size for Li+ Ion Conduction in NASICON Materials of Composition $LiMM'(PO_4)_3$; M, M′ = Ge, Ti, Sn, Hf. *J. Phys. Chem. B* **1998**, *102*, 372–375. [CrossRef]